

Journal of Materials Chemistry A

Materials for energy and sustainability

Accepted Manuscript

This article can be cited before page numbers have been issued, to do this please use: E. Gala, G. Caridad, M. Vettori, S. Royuela, M. Martínez-Fernández, J. I. Martínez, E. Salagre, E. G. Michel, F. Zamora, J. Lloret Fillol and J. L. Segura, *J. Mater. Chem. A*, 2024, DOI: 10.1039/D4TA02807D.



This is an Accepted Manuscript, which has been through the Royal Society of Chemistry peer review process and has been accepted for publication.

Accepted Manuscripts are published online shortly after acceptance, before technical editing, formatting and proof reading. Using this free service, authors can make their results available to the community, in citable form, before we publish the edited article. We will replace this Accepted Manuscript with the edited and formatted Advance Article as soon as it is available.

You can find more information about Accepted Manuscripts in the [Information for Authors](#).

Please note that technical editing may introduce minor changes to the text and/or graphics, which may alter content. The journal's standard [Terms & Conditions](#) and the [Ethical guidelines](#) still apply. In no event shall the Royal Society of Chemistry be held responsible for any errors or omissions in this Accepted Manuscript or any consequences arising from the use of any information it contains.

ARTICLE

Post-synthetic modification of Covalent Organic Frameworks with active Manganese centers for the electrocatalytic CO₂ reduction in waterReceived 00th January 20xx,
Accepted 00th January 20xx

DOI: 10.1039/x0xx00000x

Elena Gala,^{a,b,†} Geyla C. Dubed Bandomo,^{c,†} Mattia Vettori,^c Sergio Royuela,^d Marcos Martínez-Fernández,^a José I. Martínez,^e Elena Salagre,^{f,g} Enrique G. Michel,^{f,g} Félix Zamora,^{d,g,h} Julio Lloret-Fillol,^{*c,i} and José L. Segura^{*a}

The development of effective catalysts for the CO₂ reduction reaction (CO₂RR) is essential for transforming atmospheric CO₂ into valuable chemical scaffolds. While numerous catalysts have been developed for the CO₂RR, few are suitable for use in aqueous systems due to inherent design challenges. In this context, Covalent Organic Frameworks (COFs) have emerged as promising materials for CO₂RR in water, offering potential solutions to these challenges. Thanks to their porosity, high surface area and crystalline structure, COFs are excellent hosts for single-atom catalysts (SACs), enabling the immobilization of high-value species and their utilization in heterogeneous catalyzed processes. For this reason, we have explored the catalytic activity of a terpyridine-manganese complex endowed into a COF lattice, which was successfully synthesized and characterized, confirming the presence of the metal ion in the material with spectroscopic techniques such as XPS and EDS. This new material has proved to be an active heterogeneous catalyst for CO₂RR in water as solvent, finding a faradaic yield of 42 % for CO at 300 mV overpotential and 16 % of formate when 600 mV were applied. Furthermore, an *ab initio* theoretical study is included to provide a reasonable mechanism of CO₂RR towards the CO evolution pathway.

Introduction

CO₂ has become a target molecule to use as a C1 building block to synthesize high-value renewable solar fuels in the context of circular economy.^[1–3] The electrocatalytic reduction of CO₂ (CO₂RR) into valuable products such as liquid fuels can not only reduce the increase of CO₂ accumulation in the atmosphere but also lead to pathways toward new renewable chemicals and high energy density fuels.^[4] Careful design of catalyst for this transformation has delivered molecular complexes with extremely high turnover frequencies, and in many cases low

onset potentials, for C1 products such as CO, HCOOH and CH₄.^[5,6] Despite these advances, the majority of studies involve catalysts only soluble in organic solvents - a reaction medium that also facilitates high CO₂ concentrations. In contrast, heterogeneous catalysts including metals such as Cu, Au and Ag offers high current densities and stability in water, but rational design of the catalyst sites and development of catalysts remains a significant challenge.^[7] This gap underscores the need for catalyst designs that combine the efficiency and selectivity of molecular complexes with the environmental benefits and operational feasibility of heterogeneous systems.

For instance, manganese (I) tricarbonyl complexes are efficient catalysts in the CO₂RR to generate CO with good Faradaic yields in protic organic media. However, these complexes generally suffer from poor solubility in water and recyclability. The catalysts heterogenization has been a long-standing strategy to mitigate this problems, improving the stability of molecular catalysts that operate in the homogeneous phase.^[8–11] To develop efficient (high turnover frequency “TOF_{max}”, low overpotential “ η ”) and robust (high turnover number “TON”) [Mn(N[^]N)(CO)₃X]-based catalysts for CO₂ reduction, the immobilization in a heterogeneous fashion at a solid-state interface has been explored.^[12–15] The heterogenization of well-defined catalysts could be prepared by immobilizing them on conducting and semiconducting substrates,^[16–18] and porous polymers^[19] among others.^[20] Some of these strategies to improve the stability of the [Mn(N[^]N)(CO)₃X]-based catalysts are included in Figure 1.^[13,16–19,21–24]

^a Departamento de Química Orgánica I, Facultad de CC. Químicas, Universidad Complutense de Madrid, 28040 Madrid, Spain. E-mail: segura@ucm.es

^b Chemical and Environmental Technology Department, Rey Juan Carlos University, Móstoles, 28933, Spain.

^c Institute of Chemical Research of Catalonia (ICIQ), The Barcelona Institute of Science and Technology, Tarragona 43007, Spain; Email: jlloret@iciq.es

^d Departamento de Inorgánica, Facultad de Ciencias, Universidad Autónoma de Madrid, Campus de Cantoblanco - Crta. Colmenar, Madrid 28049, Spain.

^e Departamento de Materiales de baja dimensionalidad, Instituto de Ciencia de Materiales de Madrid (ICMM-CSIC), 28049 Madrid, Spain.

^f Departamento de Física de la Materia Condensada, Universidad Autónoma de Madrid, 28049, Madrid, Spain.

^g Condensed Matter Physics Center (IFIMAC), Universidad Autónoma de Madrid, 28049, Madrid, Spain.

^h Institute for Advanced Research in Chemical Sciences (IAdChem). Universidad Autónoma de Madrid, Campus de Cantoblanco. Madrid 28049, Spain

ⁱ Catalan Institution for Research and Advanced Studies (ICREA), Barcelona 08010, Spain.

[†] Elena Gala and Geyla C. Dubed Bandomo contributed equally to this work.

Electronic Supplementary Information (ESI) available: [details of any supplementary information available should be included here]. See DOI: 10.1039/x0xx00000x



Recently, a number of studies have demonstrated another route using crystalline porous materials: Covalent Organic Frameworks (COFs)^[25] and Metal–Organic Frameworks (MOFs).^[26] These frameworks have demonstrated high levels of activity for electrocatalytic CO₂ reduction when integrated with molecular electrocatalysts.^[27–32] The molecular nature of MOFs and COFs precursors facilitates the incorporation of established molecular catalysts, resulting in frameworks that often outperform their molecular counterparts in terms of efficiency, stability, and durability.^[25,26]

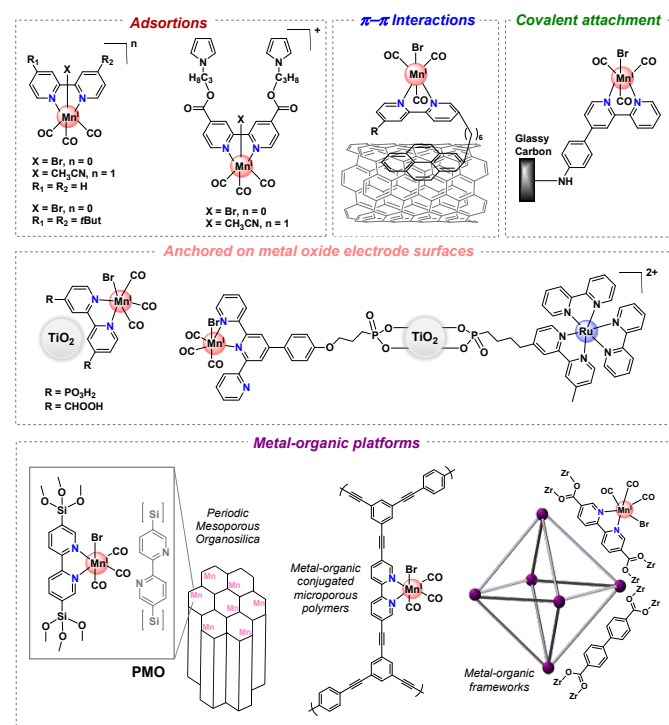


Figure 1. Selected immobilization strategies employed in manganese tricarbonyl complexes containing polypyridyl moieties.

Therefore, the use of MOFs and COFs for catalytic purposes has been extensively explored.^[33–35] The integration of molecular catalytic units into extended frameworks has often resulted in improved efficiency, stability and durability in comparison to the corresponding molecular analogues.

Among potential applications of COFs as catalysts, they stand out specially because they have been shown to be excellent precursors or hosts for single-atom catalysts (SACs).^[36,37] COFs minimize the sizes of catalytic nanoparticles and, as a result, expose more reactive sites to facilitate the mass/electron transfer at the interface and to achieve high catalytic reactivity.^[38] In this context, the interest of application of COFs for CO₂RR has started to be explored and, as a result, porphyrins, phthalocyanines and bipyridine-based complexes have been integrated as building blocks into COFs or MOFs for CO₂RR.^[2,29,47–52,39–46]

Combining the merits of heterogeneous and homogeneous catalysts, the reticular chemistry endows the framework materials with high surface areas, porous structures, and potential rational tailored for optimizing CO₂RR performance.^[38,53] Such an approach has significant advantages as it provides materials with well-defined, tunable, catalytic sites in a stable heterogenized form. Recently, a new CO₂ reduction catalyst by loading single-atom centers, {*fac*-Mn(CO)₃S} within a bipyridyl-inspired COF with 10 times higher catalytic activity than that obtained for the equivalent manganese-based molecular catalyst and access to key catalytic intermediates within a COF matrix has been published.^[54]

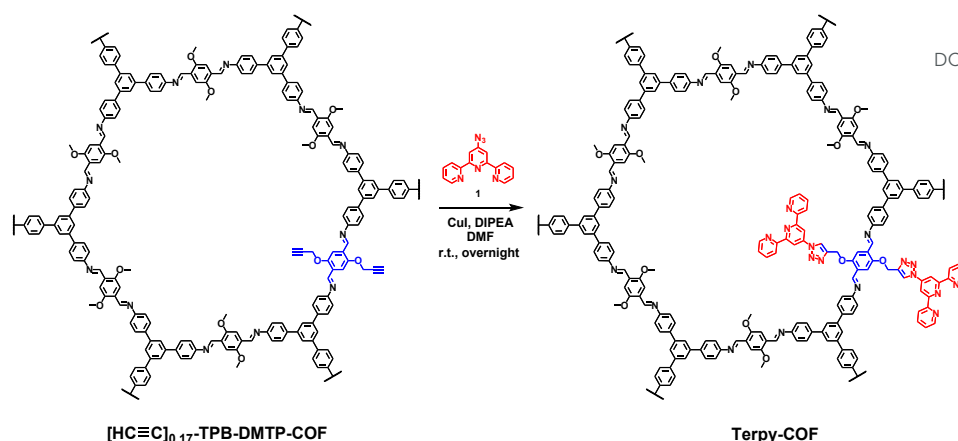
In this context, herein, we report on the synthesis, characterization and electrochemical evaluation for CO₂ reduction of a novel *fac*-[Mn(bpy)(CO)₃Br]-terpyridine type 2D COF (**Mn@Terpy-COF**). The synthesized materials have been characterized by inductively coupled plasma optical emission spectrometry (ICP-OES), thermogravimetric analysis (TGA), infrared spectroscopy (IR), carbon-13 cross-polarization magic angle spinning nuclear magnetic resonance (¹³C-CP/MAS NMR), scanning electron microscopy–energy dispersive X-ray spectroscopy (SEM–EDX), transmission electron microscopy (TEM), powder X-ray diffraction (PXRD), X-ray photoelectron spectroscopy (XPS) and X-ray absorption spectroscopy (XAS).

Results and discussion

Synthesis and characterization of Terpy-COF

A COF doped with terpyridine moieties, **Terpy-COF**, has been prepared by covalently linking azidoterpyridine **1** with a COF endowed with reactive alkyne moieties, [HC≡C]_{0.17}-TPB-DMTP-COF,^[55] via copper catalyzed [3+2] cycloaddition reaction (Scheme 1). The structural characterization of the new COF has been elucidated and compared with that of the precursor COF endowed with alkyne moieties. The completeness of the reaction between the azides and the alkyne was confirmed by Fourier transform infrared (FT-IR) spectroscopy (Figure S5) and Solid-state Cross-Polarization Magic Angle Spinning Carbon-13 Nuclear Magnetic Resonance (¹³C-CP/MAS-NMR) (Figure 2a). Thus, the diagnostic ν(C=N) stretching band at 1618 cm⁻¹ remain almost unaltered in the FT-IR spectra after the cycloaddition reaction.^[56] On the other hand, ¹³C-CP/MAS-NMR spectrum evidences the efficient transformation as revealed by the vanishing of the signals corresponding to the alkyne group at 79 and 72 ppm (Figure 2a). The remaining aliphatic signal at 54 ppm is attributed to the methoxy groups of the COF skeleton. Introduction of the terpyridine fragment was also confirmed analyzing the aromatic region. First, quaternary pyridine C=N carbons were localized together with the rest of C=N carbons of the COF in the signal at 154 ppm, which appears broader than in starting material [HC≡C]_{0.17}-TPB-DMTP-COF (Figure S3). Introduction of pyridine fragment was not only evidenced by the widening of the signal corresponding to C=N, but also by the





Scheme 1: Synthesis of **Terpy-COF** from **[HC≡C]_{0.17}-TPB-DMTP-COF**

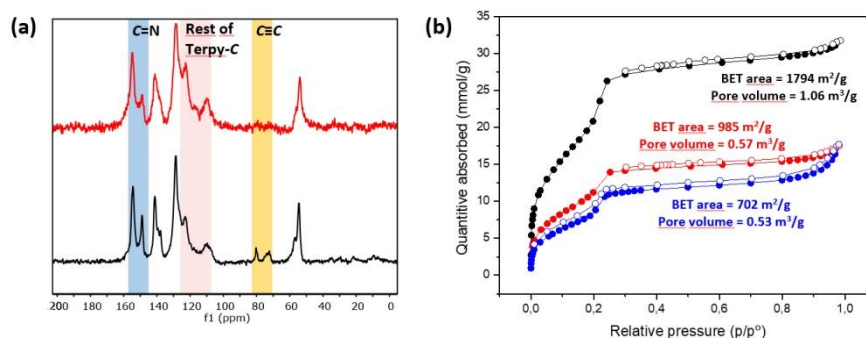


Figure 2. Comparative (a) ¹³C CP/MAS NMR patterns of **[HC≡C]_{0.17}-TPB-DMTP-COF** (black) and **Terpy-COF** (red), (b) N₂ (77 K) sorption isotherms of **[HC≡C]_{0.17}-TPB-DMTP-COF** (black), **Terpy-COF** (red) and **Mn@Terpy-COF** (blue).

appearance of a new signal (observed as a shoulder) at 117 ppm and enhancement of relative intensities of signals at 122 and 109 ppm (Figure S3), which corresponds to chemical shifts of terpyridine C3'(5'), C3(3'') and C5(5'') carbons (Figures S2 and S4). Chemical shifts of the rest of anisochronous nuclei correspond well with that expected for the structure of the COF core, those of the triazole rings and that of the terpyridine system. It should be highlighted that neither the precursor **[HC≡C]_{0.17}-TPB-DMTP-COF** nor the final cycloaddition product exhibited FTIR or ¹³C-CP-MAS-NMR signals of the starting materials corresponding to aldehyde or amine functionalities. The introduction of the terpyridine fragment into the pore resulted, as it was expected, in a decrease of the Brunauer-Emmett-Teller (BET) surface area of **Terpy-COF** (985 m²/g) in comparison with that of the starting material **[HC≡C]_{0.17}-TPB-DMTP-COF** (1794 m²/g) (Figure 2b). N₂ sorption isotherms at 77 K also revealed a reduction of pore volume (from 1.06 cm³/g to 0.57 cm³/g at 0.95 p/p⁰) and pore size distribution, calculated by NLDFT, Figure S7). These data, together with the IV-type isotherm obtained, evidence the mesoporous nature of the **Terpy-COF**.^[55]

Morphological characterization of **Terpy-COF** and **[HC≡C]_{0.17}-TPB-DMTP-COF** have been carried by using Scanning Electron Microscopy (SEM). SEM micrographs revealed that the mild conditions of the copper catalyzed click reaction did not

significantly alter the morphology of the COF and therefore **[HC≡C]_{0.17}-TPB-DMTP-COF** and **Terpy-COF** exhibit almost identical rodlike morphologies. (Figures S8 and S9).

X-ray powder diffraction (PXRD) analysis of **Terpy-COF** revealed a high degree of crystallinity, with six distinctive diffraction peaks which almost replicate that previously observed for **[HC≡C]_{0.17}-TPB-DMTP-COF** with an eclipsed AA stacking (Figure 3a).^[55] The most intense diffraction maxima, at 2.90°, had an excellent FWHM value of 0.2303° and corresponds to (100) facet.^[57] The other peaks appeared at 4.95°, 5.70°, 7.54°, 9.83° and 25.20° and can be assigned to (110), (200), (210), (220) and (001) reflections according to that previously reported for **[HC≡C]_{0.17}-TPB-DMTP-COF**.^[55] With the aim to confirm the macromolecular crystal structure of **Terpy-COF**, we have conducted an extensive battery of DFT-based calculations using a combination of Gaussian 16 C.01^[58] and QUANTUM ESPRESSO^[59] software packages to determine the crystalline structures of **TPB-DMTP-COF** and **Terpy-COF** in this study (further computational details in SI). The simulations revealed purely hexagonal symmetry for all crystal structures, with monolayer lattice parameters ranging from 37.57 to 37.72 Å (Figure 3). We studied the preferred stacking configuration for **TPB-DMTP-COF** and **Terpy-COF**. In both cases, the AA eclipsed configuration was found to be preferential, with very similar interlayer distances of 3.61 and 3.72 Å (Figure 3). The



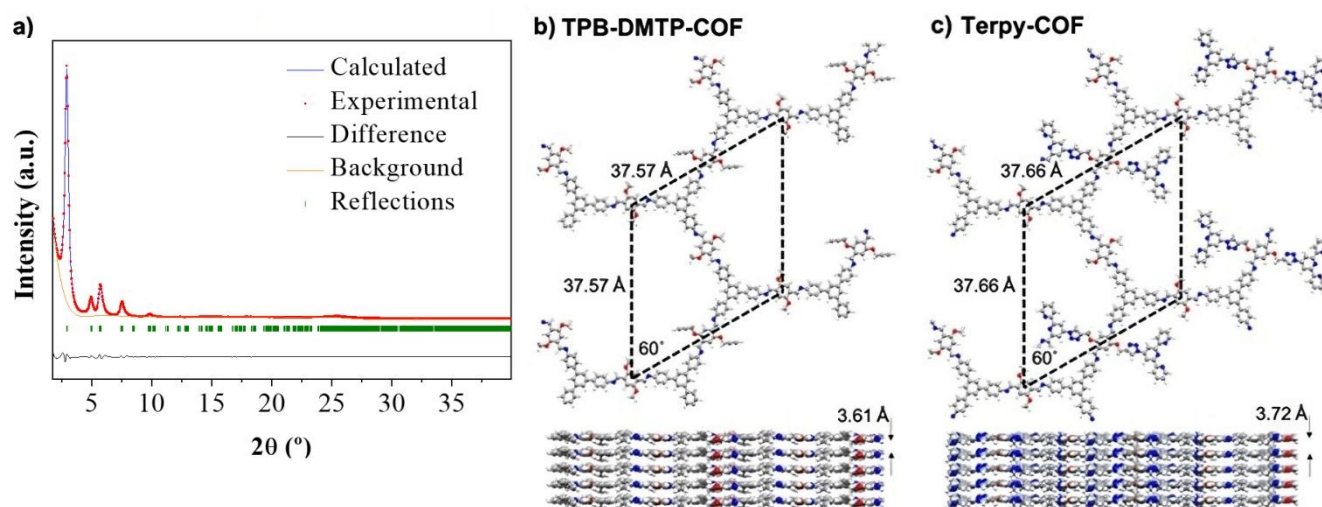


Figure 3. a) Comparison between the experimental (red) and the theoretically simulated (blue) diffractograms obtained from the resulting optimized structures for $[\text{HC}\equiv\text{C}]_{0.17}\text{-TPB-DMTP-COF}$ and **Terpy-COF** (practically identical). Experimental diffractogram has been refined (Rietveld refinement) with parameters $R_{wp}=4.54\%$ and $R_2\ 3.08\%$. b) and c) Top and side pictorial views of the structures, indicating the resulting optimized unit cell in all cases, for the b) $[\text{HC}\equiv\text{C}]_{0.17}\text{-TPB-DMTP-COF}$ and c) **Terpy-COF**. The preferential interlaminar stacking for the $[\text{HC}\equiv\text{C}]_{0.17}\text{-TPB-DMTP-COF}$ and **Terpy-COF** is the eclipsed configuration, showing a very similar interlayer distance.

theoretical diffractograms based on optimized crystal structures (Figure 3c, practically identical for both) showed excellent agreement with experimental ones. The diffraction peaks in the simulated PXRD pattern are located at 2.803° , 4.821° , 5.605° , 7.287° , 13.677° and 24.776° in excellent agreement with the experimental evidence as showed the Rietveld refinement (Figure 3a). The simulated PXRD pattern even reproduced high-angle features, confirming the validity of structures obtained from simultaneous structure + cell DFT geometrical optimizations.

Synthesis of Mn@Terpy-COF

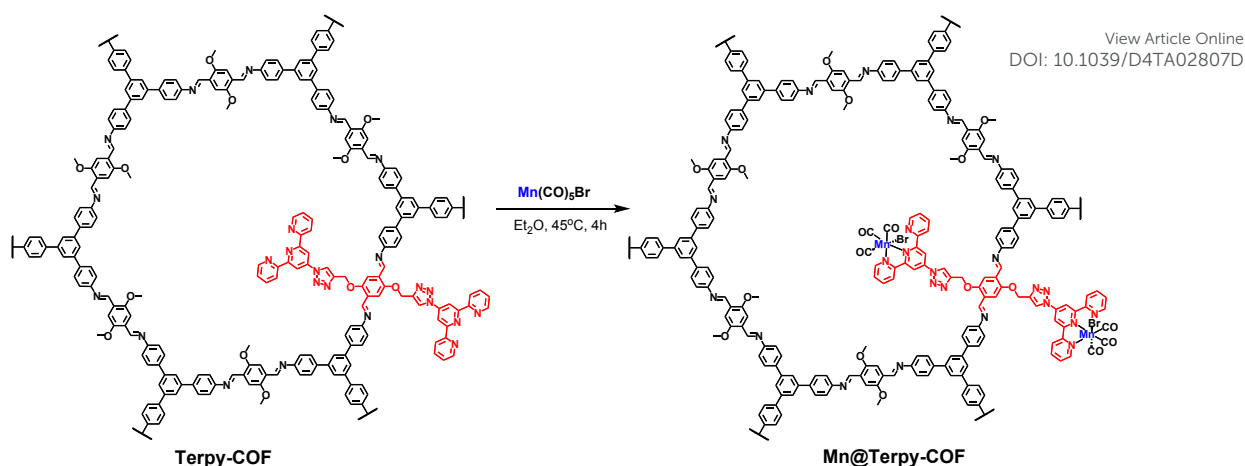
The **Terpy-COF** post-functionalization was performed by direct reaction with $\text{Mn}(\text{CO})_5\text{Br}$ at 45°C in diethyl ether for 4 h, forming **Mn@Terpy-COF** as a brown powder (Scheme 2). The amount of Mn measured by Inductively coupled plasma-optical emission spectroscopy (ICP-OES) results in an inclusion of 38 mg of Mn by g of **Terpy-COF**, accounted for $\sim 75\%$ of the COF terpyridines coordinated to Mn after de metalation.

The incorporation of $\{fac\text{-Mn}(\text{CO})_3\text{Br}\}$ fragments into the **Terpy-COF** was confirmed by ATR-FT-IR spectroscopy, showing the presence of two CO stretching frequencies at 2020 cm^{-1} and a shoulder at 1919 cm^{-1} (Figure 4). The frequency at 2020 cm^{-1} matches for the $\nu_{(\text{CO})}$ of the symmetric CO vibration of the facial tricarbonyl moiety and the unresolved broad band at 1919 cm^{-1} correspond to the symmetric and asymmetric equatorial CO vibration. This pattern is analogous to that shown by the molecular $\{fac\text{-Mn}^{\text{I}}(\kappa^2\text{-terp})(\text{CO})_3\text{Br}\}$ complex reported by

Kubiak and col.^[60] The UV-Vis spectrum (Figure S6), thermogravimetric analysis (Figure S14), PXRD (Figure S15) as well as porosity and surface area measurements (Figures 2 and S7) were also conducted to characterize the material. Powder X-ray diffraction analysis confirmed that the crystallinity of the COF was preserved after the metalation process (Figure S15). As anticipated, porosity and surface area decreased following the incorporation of the metal within the pore structure, yielding a BET surface area of $702\text{ m}^2/\text{g}$ (Figure 2) and a pore volume of $0.53\text{ cm}^3/\text{g}$ at a relative pressure of 0.95 (p/p^0 , Figure S7). These observations align with the expected reduction in porosity and pore volume upon introduction of Mn and CO moieties into the pore network, confirming the impact of these modifications on the material's structural properties.

Extensive X-ray photoemission spectroscopy (XPS) characterization study was also performed to determine the correct structure assigned **Terpy-COF** to and **Mn@Terpy-COF** (Figures S16-19). Analyzing first the starting material **Terpy-COF**, -N 1s emission peak was clearly identified and presented different components, so it was deconvoluted for a more detailed analysis. The two main components, labeled A and B, were identified at 398.5 and 399.9 eV, and an additional minor component, labeled C, was observed at 401.5 eV (Figure 5). The main component, corresponding to a binding energy of 398.5 eV, was attributed to -N= of the imine and pyridine groups. The peaks detected at 399.9 and 401.5 eV were assigned to imidazole nitrogen atoms. Specifically, the lower binding energy signal was assigned to N labeled 2 and 3 while the less intense





Scheme 2: Synthesis of **Mn@Terpy-COF** from **Terpy-COF**.

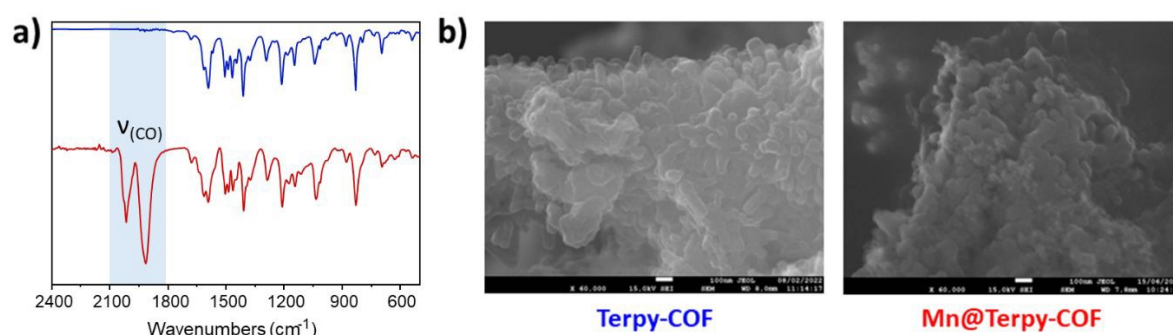


Figure 4. (a) ATR spectra $\nu_{(\text{CO})}$ at 2025 and 1915 (sh), (c) SEM of **Terpy-COF** (blue) and **Mn@Terpy-COF** (red).

crest was assigned to the nitrogen directly attached to the terpyridine fragment, labeled 1 (Figure 5). These relative positions of binding energy and intensity percentages agree with our predictions and with data from the literature. The addition of manganese to the COF caused a noticeable change in the N 1s peak area percentages and a slight displacement of the component with the highest binding energy (C) as can be seen in Figure 5. The observed percentage change of the peak is related to the shift of the binding energy of part of the terpyridine nitrogen atoms from the initial imine region (398.5 eV) to the imidazole 2 and 3 zone at 399.9 eV, which is observed broader and with a higher relative intensity. This result is consistent with what is expected for the structure of **Mn@Terpy-COF** because the nitrogens coordinated with manganese have given charge to the metal ion and appear more oxidized. On the other hand, the signal originating from Mn 2p in the **Mn@Terpy-COF** XPS spectrum shows two components (Figure S17). The major component (642 eV, 67%) is assigned to manganese coordinated to terpyridine. The minor component (646 eV, 33%) could be related to manganese in a different environment, but we discard this interpretation considering the high value of the binding energy. Instead, we attribute it to a shake-up satellite observed in other Mn coordination complexes about 4 eV higher than the main Mn 2p photoelectron line.^[61] In both compounds, **Terpy-COF** and

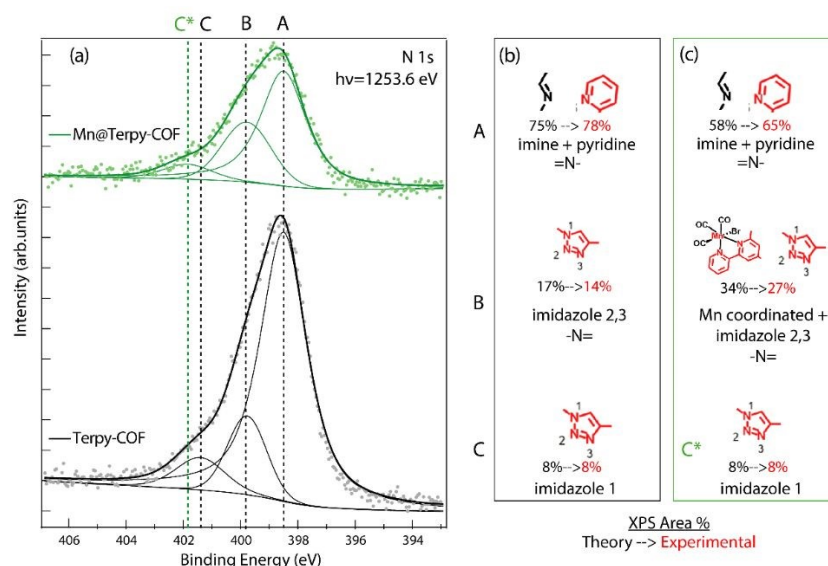
Mn@Terpy-COF, the C 1s signals are similar (Figure S18), with the major component attributed to aromatic sp^2 carbons (A label). Minor components were also identified at higher binding energies and were assigned to sp^2 carbon directly bonded to nitrogen and oxygen (B label).

Electrocatalytic CO_2 reduction in water with **Mn@Terpy-COF**

Preparation and characterization of the thin-film **Mn@Terpy-COF|NT**

In order to study the electrocatalytic activity of the **Mn@Terpy-COF**, a film of the material was deposited on the working electrode (Glassy Carbon). The immobilization was achieved by mixing the catalyst's powder with Multi-Walled Carbon Nanotubes (MWCNTs) (NT) in CH_3CN and Nafion (5% water) (1 mg:1mg:100 μL :100 μL) by sonication (15 minutes) to obtain the **Mn@Terpy-COF|NT|ink** catalytic ink. 10 μL of the dispersion were dropped onto the electrode surface and allowed to dry in the dark and under ambient conditions to yield **Mn@Terpy-COF|NT** (Figure S13) (see the experimental section for details).





View Article Online
DOI: 10.1039/D4TA02807D

Figure 5. (a) XPS spectra of 1 N 1s peaks region of **Terpy-COF** (black) and **Mn@Terpy-COF** (green). Dots correspond to experimental points and continuous lines to the deconvolution in different components and background. Vertical dotted lines indicate the binding energy positions of the components. Panels (b) and (c) show the origin of each N 1s component. Data obtained with a Mg K α (1253.6 eV) photon source.

To gain insight into the COF matrix and the electronic structure and coordination environment of the Mn centers in the catalytic ink, an XPS study was performed. The XPS analysis of **Mn@Terpy-COF|NT|ink** suspension and **Mn@Terpy-COF|NT** showed, as previously described, C 1s signals but with new very shifted components, assigned to the carbon atoms bonded to fluorine atoms present in the Nafion polymer used (component C in figure S19). In addition, a new small component of C sp^2 was observed in the **Mn@Terpy-COF|NT** XPS spectrum, in a position similar to the benzene carbon atoms of the previously described **Terpy-COF** and **Mn@Terpy-COF** (label A* in Figure S19). The similarity in the binding energy position of the previous A component and this new A* component associated with the carbon nanotubes makes it difficult to deconvolute this into two components, but the increase in the C 1s A/B component ratio is sufficient to conclude that a new component is present. In all these new materials, the signals of N 1s were barely noticeable and the signal to noise ratio was low (Not shown). In the case of Mn, the strong signal of fluorine (F 1s and KLL Auger F) is superimposed on the Mn 2p peaks (Figure S16), making it difficult to observe and analyze the Mn state.

Catalytic activity of Mn@Terpy-COF |NT for the CO₂ reduction in water.

To evaluate the electrochemical behavior and the catalytic CO₂ reduction performances of **Mn@Terpy-COF|NT** ($[Mn]_{total} = 850 \text{ nmol}\cdot\text{cm}^{-2}$), cyclic voltammetry (CV) and controlled-potential electrolysis (CPE) measurements were carried out in K₂SO₄/K₂B₄O₇ electrolyte under Ar (pH 8.2) and CO₂ (pH 7.6) atmosphere, respectively.

We started the characterization by performing CV of **Mn@Terpy-COF|NT** under Ar and CO₂ atmospheres in K₂SO₄/K₂B₄O₇ (Figure 6a). Under Ar (pH 8.2), the CV showed an irreversible cathodic wave, suggesting a catalytic hydrogen evolution reaction (HER) that was confirmed by the detection of H₂ after control potential electrolysis (see below). When the solution was saturated with CO₂ (pH 7.4), the onset of the catalytic wave shifted 360 mV to more positive potentials and the catalytic current increased 3.5-fold (j_{CO_2}/j_{Ar} at -1.3 V).

To estimate the neat CO₂ reduction activity of **Mn@Terpy-COF|NT**, CPEs of the thin film on carbon paper (CP) electrode as current collector were recorded in aqueous K₂SO₄/K₂B₄O₇ under CO₂ (pH 7.4) (See experimental section for details). CPE were carried out to benchmark the CO₂ reduction activity selectivity, and stability of the catalyst **Mn@Terpy-COF|NT** (Figure 6b, c). The generated products were analyzed by gas chromatography and ¹H-NMR. CPE at different applied potentials (from -1.1 to -1.8 V vs SCE) of **Mn@Terpy-COF|NT** ($[Mn]_{total} = 850 \text{ nmol}\cdot\text{cm}^{-2}$) showed current densities from -0.06 to $-17 \text{ mA}\cdot\text{cm}^{-2}$. The generated products were quantified (nmol/cm²) at different overpotentials (Figure 6c), the selectivity of the CO₂ reduction reaction shifted to H₂ with the increase of the overpotential. This can be attributed to the protonation of the Mn centers forming Mn-H species, which further protonation produces H₂, and due to the exacerbation of the background reaction of H₂ formation by the carbon nanotubes as previously proposed.⁵⁴ Formation of CO and HCO₂⁻ were observed from a low η of 300 mV (Figure 6b). At $\eta = 600 \text{ mV}$, **Mn@Terpy-COF|NT** generated 2000 and 2700 nmol/cm² of CO and HCO₂⁻, respectively. Although the CO obtained was insufficient to be detectable by online GC-MS, CPE



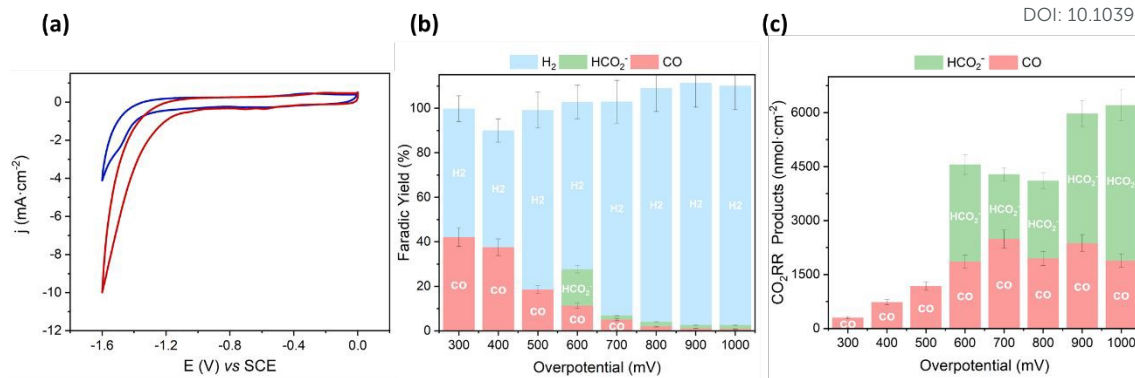


Figure 6. (a) CV on GC of **Mn@Terpy-COF|NT** ($[Mn]_{total} = 850 \text{ nmol}\cdot\text{cm}^{-2}$) in water ($K_2SO_4/K_2B_4O_7$) under Ar (blue, pH 8.2) and CO_2 (red, pH 7.4) at $10 \text{ mV}\cdot\text{s}^{-1}$. (b) Faradaic yield and (c) Generated CO_2RR products for CPEs on Carbon Paper (CP) of **Mn@Terpy-COF|NT** ($[Mn]_{total} = 850 \text{ nmol}\cdot\text{cm}^{-2}$) at different overpotentials (η). Generated products: HCO_2^- (green), CO (pink) and H_2 (blue).

experiments with $^{13}CO_2$ indicated that formate comes from the CO_2 (Figure S21).

Mn@Terpy-COF|NT electrodes showed good stability under catalytic conditions. A superimposition of linear sweep voltammetry (LSV) traces recorded before and after CPE indicates negligible catalyst decomposition (Figure 7). In general, no significant changes were observed by XPS and SEM analysis before and after electrocatalysis in water under CO_2 . EDX showed the homogeneous distribution of Mn before and after catalysis, further highlighting the robustness of **Mn@Terpy-COF|NT**.

To delve into the microscopical morphologies of **Mn@Terpy-COF|NT** before and after its test as CO_2 reduction catalyst, different SEM-EDX spectra were recorded. Deposition of the **Mn@Terpy-COF|NT/Nafion** suspension over the electrode resulted in a heterogeneous surfaced material where **Mn@Terpy-COF** is embedded in different parts of the carbon-based electrode matrix (Figure S12). This microstructure was maintained unchanged after the electrode's testing process, which is promising for a hypothetical long-time use of this dispositive as CO_2 reductive system (Figure S13). In addition, XPS spectra of the electrodes after their test as catalysts were recorded, not observing any significant change in the C 1s core level with respect to the starting material **Mn@Terpy-COF|NT** (Figure S19). However, the catalyst exhibited altered selectivity in a subsequent catalytic run, producing mainly H_2 .

Spectroelectrochemistry

SEC experiments provided further evidence of the intermediates that can be formed at different potentials in catalysis. To give some light on the catalytic activity, we have examined the material by IR-SEC, a technique that enables redox changes to be monitored by changes in the ATR spectra as a function of potential and time. Indeed, ATR-IR-SEC (Figure 8) has been previously employed to obtain structural

information on the catalytically relevant species of previous reported Mn single sites in a **COF_{bpyMn}|NT**.^[54] Considering these advantages, ATR-IR-SEC of **Mn@Terpy-COF|NT** was performed in CH_3CN (0.2 M TBAPF₆) by a stepwise decrease of the potential from 0.4 V to -1.9 V vs SCE under Ar to monitor the reduction of the precatalyst.

Before performing ATR-IR-SEC, we performed CV of **Mn@Terpy-COF|NT** in dry CH_3CN (0.2 M TBAPF₆) under Ar. The CV shows several irreversible cathodic waves in the range from -0.1 V to -1.5 V vs SCE. Besides, during the forward scan, three reoxidation processes were observed at -1.05, -0.5 and 0.6 V vs SCE, respectively. These redox transformations are similar to those observed for **Mn@Terpy** molecular complexes previously reported,^[60] suggesting an electronic similarity for the $Mn(\kappa^2\text{-tpy})(CO)_3S$ coordination between **Mn@Terpy-COF|NT** and **Mn@Terpy** as ligands.

With these considerations, ATR-IR-SEC was carried out to gain structural insights into the electrochemical activation of the **Mn@Terpy-COF|NT** precatalyst. At open-circuit potential (E_{OC}), the ATR-FT-IR of **Mn@Terpy-COF|NT** (Figure 8) showed a $\nu(CO)$ band at 2063 and a broad feature at 1982 cm^{-1} , the IR pattern corresponds to a the *-fac* arrangement within the core structure of COF, with that also match well with the pattern observed for the complex **Mn@Terpy**. This profile also agrees with the $\nu(CO)$ bands of several reported immobilized facial tricarbonyl manganese polypyridine complexes^[2] and with the previously observed for the **COF_{bpyMn}|NT**.^[54] When the potential was stepwise decreased from 0.4 to -1.6 V (vs SCE), the CO vibrations have an increase in intensities at lower energies with the evolution of the redox potential to more negative values that could be associated with a redox transformation. The ATR-IR-SEC spectra showed a decrease of the precatalyst signals with the concomitant increase of a series of bands at 1937, 1982, 1893, 1827 and 1750 cm^{-1} indicating the formation of new species. We hypothesized that after the reduction of **Mn@Terpy-COF|NT**, two different intermediates contributed to the spectra, the dimer and the anionic species



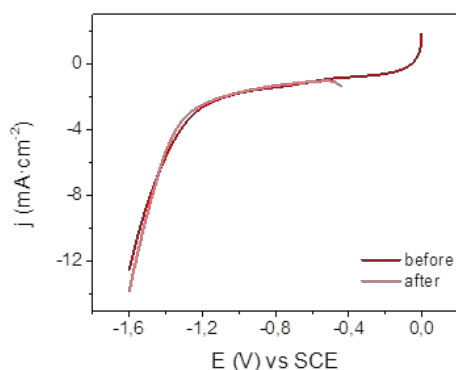


Figure 7. Linear Sweep Voltammetry of **Mn@Terpy-COF|NT** ($[\text{Mn}]_{\text{total}} = 850 \mu\text{mol}\cdot\text{cm}^{-2}$) on CP at $10 \text{ mV}\cdot\text{s}^{-1}$ before and after CPE at -1.3 V vs SCE in water $\text{K}_2\text{SO}_4/\text{K}_2\text{B}_4\text{O}_7$ under CO_2 .

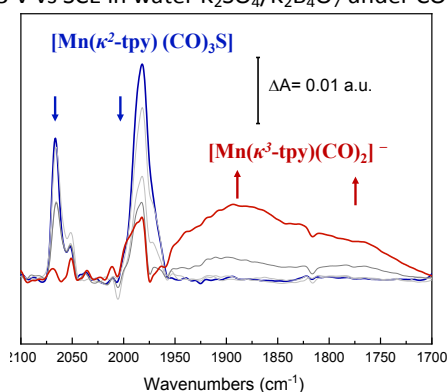


Figure 8. ATR-SEC spectra of **Mn@Terpy-COF** in 0.2 M $\text{TBAPF}_6/\text{CH}_3\text{CN}$ under Ar saturation. Red curve describes the final spectra, whereas grey lines refer to selected intermediate spectra. Blue curve is the starting catalyst.

(Figure 8), similar to the intermediates detected for the molecular **Mn@Terpy**.^[60]

Computed CO_2 Reduction Reaction (CO_2RR) Mechanism

As a proof-of-concept, a large battery of ab initio theoretical calculations was carried out to obtain a viable mechanism for the CO_2RR towards the CO evolution as reaction product (see further details in SI). Formate evolution has not been theoretically analyzed since its faradaic yield (FY) is significantly lower than the CO one for all voltages applied.

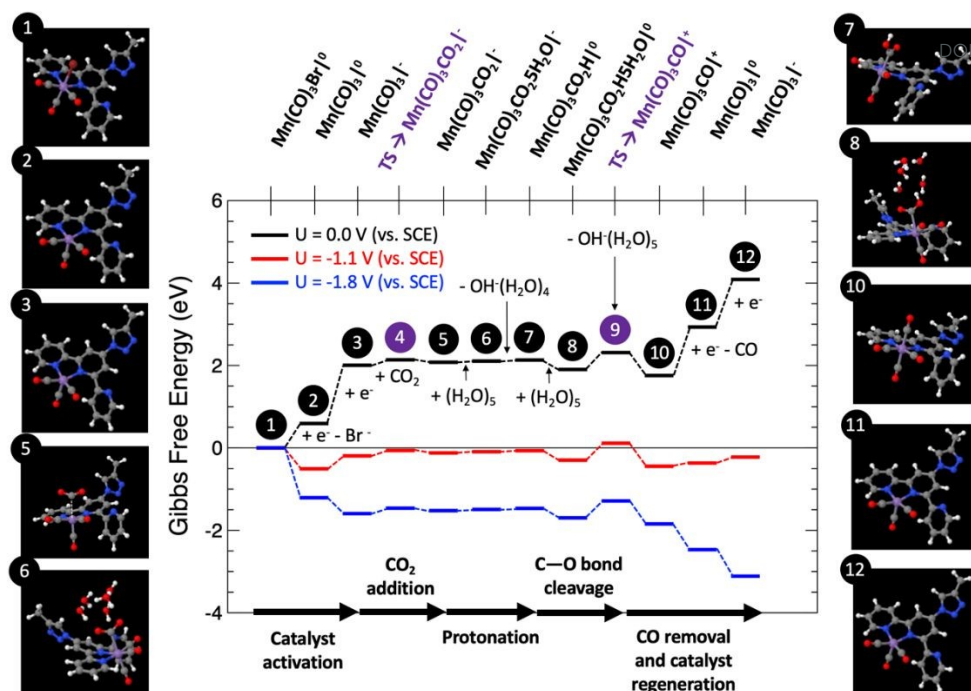
Figure 9 shows the computed Gibbs free energy diagram for the proposed mechanism, for which all the structures were fully optimized in water solution, for externally applied voltages vs. SCE mimicking the voltage range explored in the experiments: $U=0, -1.1$ and -1.8 V .

Catalyst activation. The first step **(1)** depicts the organometallic unit as participating in the COF system, in which the Mn atom has an oxidation state of +1 and a six-folded coordination with a pseudo-octahedral structure. After two sequential one-electron reductions, two electrons are transferred to the Mn center for the catalyst activation by a net free energy change at $U=0 \text{ V}$ of $+2.01 \text{ eV}$. The first one-electron reduction leads to the barrierless Br^- release towards the formation of **(2)**. After that step, **(2)** can be easily electro-reduced into **(3)**, with a net free energy gain of $+1.42 \text{ eV}$. After these two electro-reductions the two additional electrons are located over the $d_{xy}(\text{Mn})$ orbitals.^[62]

CO_2 adsorption and protonation. Once the active species **(3)** are formed, CO_2 can anchor in the Mn vacant site with a computed low energy barrier of 0.26 eV **(4)**, to finally form the Mn- CO_2 intermediate **(5)** with a net free energy change of around $+0.07 \text{ eV}$ (endergonic) at $U=0 \text{ V}$, and a bond-length Mn-C of around 3.16 \AA . After this step, the reaction proceeds by the protonation of the CO_2 ligand. This process has been modelled by the explicit inclusion of a $(\text{H}_2\text{O})_5$ cluster in a chair configuration as previously reported,^[63] which leads the water cluster to coordinate with CO_2 to yield **(6)**. In this step a transfer of a proton is produced from the water cluster to the C-O unit to form **(7)**, followed by the subsequent release of $\text{OH}^-(\text{H}_2\text{O})_4$ with a slight net free energy change of $+0.03 \text{ eV}$ (endergonic) at $U=0 \text{ V}$.

CO release and catalyst regeneration. An explicit $(\text{H}_2\text{O})_5$ water cluster can coordinate again with **(7)** to exergonically form **(8)** ($\Delta G = -0.23 \text{ eV}$), and capturing an OH^- by subsequent release of $\text{OH}^-(\text{H}_2\text{O})_5$ with a slight net free energy loss of -0.15 eV leading to the positively charged $\text{Mn}(\text{CO})_3\text{CO}^+$ unit **(10)** by surmounting an associated energy barrier of 0.41 eV **(9)**. From this step the CO release is produced spontaneously by a synergistic electro-reduction with an associated net free energy gain of $+1.18 \text{ eV}$ at $U=0 \text{ V}$ to yield **(11)**. Finally, in order to regenerate the catalyst, **(11)** can be electro-reduced ($\Delta G = +1.16 \text{ eV}$) to regenerate active species **(3)**.





View Article Online
10.1039/D4TA02807D

Figure 9. Computed Gibbs free energy diagram (in eV) for the CO₂RR towards CO evolution at different applied voltages of U=0 (black path), -1.1 (red path) and -1.8 V (blue path) vs. SCE. Calculated geometries of all the intermediates are shown numbered according to the reaction path steps, indicating each sub-reaction of the mechanistic path.

Figure 9 reveals that at U = 0 V vs. SCE the mechanism is far from being thermodynamically viable, particularly due to the sub-reactions involving the one-electron reductions. Starting from the U=0 V profile we have computed the Gibbs free energy paths at U=-1.1 and -1.8 V vs. SCE (see Fig. 9), voltage range experimentally explored. Interestingly, at U = -1.1 V the whole reaction results already exergonic by around -0.11 eV, being the C—O bond cleavage and subsequent OH⁻ abstraction (step 9) the reaction limiting step, with a net barrier of 0.71 eV, in excellent agreement with the experimental evidence. Finally, at U = -1.8 V the whole reaction is clearly exergonic by < -3 eV. For this case, once again, the C—O bond cleavage and subsequent OH⁻ abstraction is the reaction limiting step, since it is not linked to the externally applied potential, yielding a net barrier of 0.41 eV, 0.3 eV lower than for the U = -1.1 V case, so justifying the CO production increase. Thus, the atomistic mechanism theoretically proposed clearly predicts the activation of the CO₂ reduction/CO evolution channel for the voltage window experimentally explored.

Conclusions

A novel **Mn@Terpy-COF** has been synthesized from [HC≡C]_{0.17}-TPB-DMTP-COF following a pathway consistent in the introduction of a terpyridine fragment into the macromolecular material by CuAAC reaction followed by the complexation of the ligand with manganese. This new **Mn@Terpy-COF** has been shown to be an active catalyst for the electrochemical reduction

of CO₂ in water. The spectroscopic characterization of **Mn@Terpy-COF** by IR shows that the Mn center has a fac coordination environment, homologous to the molecular complex **Mn@Terpy** and the **COF_{bpy}Mn**. XPS analysis also evidences the formation of **Mn@Terpy-COF**. Positive shifts in the onset potentials and increases in current are observed in the CV of the frameworks when the atmosphere is changed from Ar to CO₂. **Mn@Terpy-COF** reduces CO₂ to CO with FY of 42% at only 300 mV of overpotential. In addition, a FY of 16% was observed for formate production at 600 mV of overpotential.

Author Contributions

Conceptualization: J.L.S., F.Z., J.L.-F. Investigation: E.G., G.C.D.B., S.R., M.M.F., E.S. Methodology: E.G., G.C.D.B., S.R., J.I.M., E.S. Writing – original draft: E.G., G.C.D.B., M.M.F., J.I.M., E.S. Writing – review and editing: E.G., M.M.F., E.S., F.Z., J.I.M. E.G.M., J.L.-F., J.L.S. Visualization: All the authors. Project administration and supervision: J.I.M., E.G.M., F.Z., J.L.-F., J.L.S.

Conflicts of interest

There are no conflicts to declare.



Acknowledgements

This work was financially supported by Research Project TED2021-129886B-C43, TED 2021-129886B-C42 and TED2021-132790B-I00 granted by MCIN/AEI/10.13039/501100011033 and the European Union NextGeneration EU/ PRTR; and Research Project PID2022-138908NB-C33, PID 2022-138908NBC31 and PID2022-140142OB-I00 granted by MCIN/AEI/10.13039/501100011033/ and FEDER A way to make Europe and the Spanish MICINN (PDC 2022-133498-I00). J.L.S. acknowledges the MICIIN for the REDES project "RED2022-134503-T". J.L.-F. acknowledge Fundación Ramón Areces for the project ElectroFuel and Spanish MCINN for PDC2022-133451-I00. JIM acknowledges financial support by Spanish MCINN (Grants PID2020-113142RB-C21, PLEC2021-007906 and TED2021-129416A-I00), Comunidad de Madrid (Grant Y2020/NMT-6469), and CSIC (Grant BILAT23033). ES and EGM acknowledge financial support by Spanish MICINN (Grant PID2021-123295NB-I00). J.L.-F. and G.C.D.B. also acknowledge the financial support of the ICIQ Foundation, the CERCA Program/Generalitat de Catalunya, MCIN through Severo Ochoa Excellence Accreditation 2020 - 2023 (CEX2019-000925-S, MIC/AEI), AGAUR (2021 SGR 01260), Excellence in R&D (CEX 2018-000805-M). This work was also supported by the "María de Maeztu" Programme for Units of Excellence in R&D (CEX 2018-000805-M). and the Comunidad de Madrid (MAD2D-CM and TEC-2024/ECO-332) and MICINN (Planes complementarios, Materiales Avanzados). FZ also acknowledges support from the European Innovation Council under grant Agreement 101047081 (EVA).

References

- [1] O. S. Bushuyev, P. De Luna, C. T. Dinh, L. Tao, G. Saur, J. van de Lagemaat, S. O. Kelley, E. H. Sargent, *Joule* **2018**, *2*, 825–832.
- [2] S. Fernandez, G. C. Dubed Bandomo, J. Lloret-Fillol, in *Manganese Catal. Org. Synth.*, **2021**, pp. 137–181.
- [3] T. H. Wang, C. Di Dong, J. Y. Lin, C. W. Chen, J. S. Chang, H. Kim, C. P. Huang, C. M. Hung, *Sustain.* **2021**, *13*, 1–31.
- [4] J. Resasco, A. T. Bell, *Trends Chem.* **2020**, *2*, 825–836.
- [5] N. Jeyachandran, W. Yuan, C. Giordano, *Molecules* **2023**, *28*, DOI 10.3390/molecules28083504.
- [6] Z. Li, B. Han, W. Bai, G. Wei, X. Li, J. Qi, D. Liu, Y. Zheng, L. Zhu, *Sep. Purif. Technol.* **2023**, *324*, 124528.
- [7] Z. Zhang, Z. Yang, L. Liu, Y. Wang, S. Kawi, *Adv. Energy Mater.* **2023**, *13*, DOI 10.1002/aenm.202301852.
- [8] C. U. J. Pittman, L. R. Smith, *J. Am. Chem. Soc.* **1975**, *97*, 341–344.
- [9] D. Yang, B. Ni, X. Wang, *Adv. Energy Mater.* **2020**, *10*, 2001142.
- [10] A. Wagner, C. D. Sahm, E. Reisner, *Nat. Catal.* **2020**, *3*, 775–786.
- [11] M. A. W. Lawrence, C. Thompson, S. C. Lorraine, *Inorganica Chim. Acta* **2024**, *560*, 121829.
- [12] D. C. Grills, M. Z. Ertem, M. McKinnon, K. T. Ngo, J. Rochford, *Coord. Chem. Rev.* **2018**, *374*, 173–217.
- [13] B. Reuillard, K. H. Ly, T. E. Rosser, M. P. Kuenne, P. Zebger, E. Reisner, *J. Am. Chem. Soc.* **2017**, *139*, 14425–14435.
- [14] J. J. Walsh, M. Forster, C. L. Smith, G. Neri, R. J. Potter, A. J. Cowan, *Phys. Chem. Chem. Phys.* **2018**, *20*, 6811–6816.
- [15] S. Fernández, G. C. Dubed Bandomo, J. Lloret-Fillol, in *Recent Highlights II* (Eds.: R. van Eldik, C.D.B.T.-A. in I.C. Hubbard), Academic Press, **2022**, pp. 301–353.
- [16] S. Sato, K. Saita, K. Sekizawa, S. Maeda, T. Morikawa, *ACS Catal.* **2018**, *8*, 4452–4458.
- [17] X. Zhang, Z. Wu, X. Zhang, L. Li, Y. Li, H. Xu, X. Li, X. Yu, Z. Zhang, Y. Liang, H. Wang, *Nat. Commun.* **2017**, *8*, 14675.
- [18] E. Torralba-Peñalver, Y. Luo, J.-D. Compain, S. Chardon-Noblat, B. Fabre, *ACS Catal.* **2015**, *5*, 6138–6147.
- [19] C. L. Smith, R. Clowes, R. S. Sprick, A. I. Cooper, A. J. Cowan, *Sustain. Energy Fuels* **2019**, *3*, 2990–2994.
- [20] O. Piermatti, R. Abu-Reziq, L. Vaccaro, in *Catal. Immobil.*, **2020**, pp. 1–22.
- [21] J. J. Walsh, C. L. Smith, G. Neri, G. F. S. Whitehead, C. M. Robertson, A. J. Cowan, *Faraday Discuss.* **2015**, *183*, 147–160.
- [22] G. Neri, P. M. Donaldson, A. J. Cowan, *Phys. Chem. Chem. Phys.* **2019**, *21*, 7389–7397.
- [23] H. Fei, M. D. Sampson, Y. Lee, C. P. Kubiak, S. M. Cohen, *Inorg. Chem.* **2015**, *54*, 6821–6828.
- [24] J. J. Walsh, G. Neri, C. L. Smith, A. J. Cowan, *Organometallics* **2019**, *38*, 1224–1229.
- [25] K. T. Tan, S. Ghosh, Z. Wang, F. Wen, D. Rodríguez-San-Miguel, J. Feng, N. Huang, W. Wang, F. Zamora, X. Feng, A. Thomas, D. Jiang, *Nat. Rev. Methods Prim.* **2023**, *3*, 1.
- [26] Q. Zhang, S. Yan, X. Yan, Y. Lv, *Sci. Total Environ.* **2023**, *902*, DOI 10.1016/j.scitotenv.2023.165944.
- [27] Q. J. Wu, J. Liang, Y. B. Huang, R. Cao, *Acc. Chem. Res.* **2022**, *55*, 2978–2997.
- [28] S. Huang, K. Chen, T. T. Li, *Coord. Chem. Rev.* **2022**, *464*, 214563.
- [29] Y. Fan, M. Chen, N. Xu, K. Wang, Q. Gao, J. Liang, Y. Liu, *Front. Chem.* **2022**, *10*, 1–8.
- [30] Y. Guan, J. Lai, G. Xu, *ChemElectroChem* **2021**, *8*, 2764–2777.
- [31] C. Li, Y. Ji, Y. Wang, C. Liu, Z. Chen, J. Tang, Y. Hong, X. Li, T. Zheng, Q. Jiang, C. Xia, *Applications of Metal–Organic Frameworks and Their Derivatives in Electrochemical CO₂ Reduction*, **2023**.
- [32] J. Wang, Y. Zhang, Y. Ma, J. Yin, Y. Wang, Z. Fan, *ACS Mater. Lett.* **2022**, *4*, 2058–2079.
- [33] S. Abednatanzi, M. Najafi, P. Gohari Derakhshandeh, P. Van Der Voort, *Coord. Chem. Rev.* **2022**, *451*, 214259.
- [34] F. Gao, R. Yan, Y. Shu, Q. Cao, L. Zhang, *RSC Adv.* **2022**, *12*, 10114–10125.
- [35] H. Y. Cheng, T. Wang, *Adv. Synth. Catal.* **2021**, *363*, 144–193.
- [36] M. N. Hossain, L. Zhang, R. Neagu, E. Rassachack, *Free-Standing Single-Atom Catalyst-Based Electrodes for CO₂ Reduction*, Springer Nature Singapore, **2024**.
- [37] I. Barlocco, G. Di Liberto, G. Pacchioni, *Energy Adv.* **2023**, *2*, 1022–1029.



- [38] C. S. Diercks, Y. Liu, K. E. Cordova, O. M. Yaghi, *Nat. Mater.* **2018**, *17*, 301–307.
- [39] G. Centi, S. Perathoner, *Catal. Today* **2009**, *148*, 191–205.
- [40] L. Ye, J. Liu, Y. Gao, C. Gong, M. Addicoat, T. Heine, C. Wöll, L. Sun, *J. Mater. Chem. A* **2016**, *4*, 15320–15326.
- [41] C. S. Diercks, S. Lin, N. Kornienko, E. A. Kapustin, E. M. Nichols, C. Zhu, Y. Zhao, C. J. Chang, O. M. Yaghi, *J. Am. Chem. Soc.* **2018**, *140*, 1116–1122.
- [42] H. Liu, J. Chu, Z. Yin, X. Cai, L. Zhuang, H. Deng, *Chem* **2018**, *4*, 1696–1709.
- [43] C.-L. Yao, J.-C. Li, W. Gao, Q. Jiang, *Chem. – A Eur. J.* **2018**, *24*, 11051–11058.
- [44] N. Huang, K. H. Lee, Y. Yue, X. Xu, S. Irle, Q. Jiang, D. Jiang, *Angew. Chemie Int. Ed.* **2020**, *59*, 16587–16593.
- [45] M.-D. Zhang, D.-H. Si, J.-D. Yi, S.-S. Zhao, Y.-B. Huang, R. Cao, *Small* **2020**, *16*, 2005254.
- [46] M. Lu, M. Zhang, C.-G. Liu, J. Liu, L.-J. Shang, M. Wang, J.-N. Chang, S.-L. Li, Y.-Q. Lan, *Angew. Chemie Int. Ed.* **2021**, *60*, 4864–4871.
- [47] B. Han, X. Ding, B. Yu, H. Wu, W. Zhou, W. Liu, C. Wei, B. Chen, D. Qi, H. Wang, K. Wang, Y. Chen, B. Chen, J. Jiang, *J. Am. Chem. Soc.* **2021**, *143*, 7104–7113.
- [48] H. Dong, M. Lu, Y. Wang, H.-L. Tang, D. Wu, X. Sun, F.-M. Zhang, *Appl. Catal. B Environ.* **2022**, *303*, 120897.
- [49] M. Liu, Y.-R. Wang, H.-M. Ding, M. Lu, G.-K. Gao, L.-Z. Dong, Q. Li, Y. Chen, S.-L. Li, Y.-Q. Lan, *Sci. Bull.* **2021**, *66*, 1659–1668.
- [50] Y. Bochlin, L. Ezuz, Y. Kadosh, D. Benjamin, Y. Mordekovitz, S. Hayun, E. Korin, A. Bettelheim, *ACS Appl. Energy Mater.* **2021**, *4*, 10033–10041.
- [51] E. M. Johnson, R. Haiges, S. C. Marinescu, *ACS Appl. Mater. Interfaces* **2018**, *10*, 37919–37927.
- [52] D. A. Popov, J. M. Luna, N. M. Orchanian, R. Haiges, C. A. Downes, S. C. Marinescu, *Dalt. Trans.* **2018**, *47*, 17450–17460.
- [53] J. Li, D. Zhao, J. Liu, A. Liu, D. Ma, *Molecules* **2020**, *25*, DOI 10.3390/molecules25102425.
- [54] G. C. Dubed Bandomo, S. S. Mondal, F. Franco, A. Bucci, V. Martin-Diaconescu, M. A. Ortuño, P. H. van Langevelde, A. Shafir, N. López, J. Lloret-Fillol, *ACS Catal.* **2021**, *11*, 7210–7222.
- [55] H. Xu, J. Gao, D. Jiang, *Nat. Chem.* **2015**, *7*, 905–912.
- [56] Q. Xu, S. Tao, Q. Jiang, D. Jiang, *Angew. Chemie Int. Ed.* **2020**, *59*, 4557–4563. DOI: 10.1039/D4TA02807D
- [57] X. Li, J. Qiao, S. W. Chee, H.-S. Xu, X. Zhao, H. S. Choi, W. Yu, S. Y. Quek, U. Mirsaidov, K. P. Loh, *J. Am. Chem. Soc.* **2020**, *142*, 4932–4943.
- [58] M. J. Frisch, G. W. Trucks, H. B. Schlegel, G. E. Scuseria, M. a. Robb, J. R. Cheeseman, G. Scalmani, V. Barone, G. a. Petersson, H. Nakatsuji, X. Li, M. Caricato, a. V. Marenich, J. Bloino, B. G. Janesko, R. Gomperts, B. Mennucci, H. P. Hratchian, J. V. Ortiz, a. F. Izmaylov, J. L. Sonnenberg, Williams, F. Ding, F. Lipparini, F. Egidi, J. Goings, B. Peng, A. Petrone, T. Henderson, D. Ranasinghe, V. G. Zakrzewski, J. Gao, N. Rega, G. Zheng, W. Liang, M. Hada, M. Ehara, K. Toyota, R. Fukuda, J. Hasegawa, M. Ishida, T. Nakajima, Y. Honda, O. Kitao, H. Nakai, T. Vreven, K. Throssell, J. a. Montgomery Jr., J. E. Peralta, F. Ogliaro, M. J. Bearpark, J. J. Heyd, E. N. Brothers, K. N. Kudin, V. N. Staroverov, T. a. Keith, R. Kobayashi, J. Normand, K. Raghavachari, a. P. Rendell, J. C. Burant, S. S. Iyengar, J. Tomasi, M. Cossi, J. M. Millam, M. Klene, C. Adamo, R. Cammi, J. W. Ochterski, R. L. Martin, K. Morokuma, O. Farkas, J. B. Foresman, D. J. Fox, **2016**, Gaussian 16, Revision C.01, Gaussian, Inc., Wallin.
- [59] P. Giannozzi, S. Baroni, N. Bonini, M. Calandra, R. Car, C. Cavazzoni, D. Ceresoli, G. L. Chiarotti, M. Cococcioni, I. Dabo, A. Dal Corso, S. de Gironcoli, S. Fabris, G. Fratesi, R. Gebauer, U. Gerstmann, C. Gougoussis, A. Kokalj, M. Lazzeri, L. Martin-Samos, N. Marzari, F. Mauri, R. Mazzarello, S. Paolini, A. Pasquarello, L. Paulatto, C. Sbraccia, S. Scandolo, G. Sclauzero, A. P. Seitsonen, A. Smogunov, P. Umari, R. M. Wentzcovitch, *J. Phys. Condens. Matter* **2009**, *21*, 395502.
- [60] C. W. MacHan, C. P. Kubiak, *Dalt. Trans.* **2016**, *45*, 17179–17186.
- [61] R. Gostynski, J. Conradie, E. Erasmus, *RSC Adv.* **2017**, *7*, 27718–27728.
- [62] C. Ci, J. Zang, L. Chao, K. Xiao, X. Peng, *Inorganica Chim. Acta* **2023**, *549*, 121419.
- [63] C. Riplinger, M. D. Sampson, A. M. Ritzmann, C. P. Kubiak, E. A. Carter, *J. Am. Chem. Soc.* **2014**, *136*, 16285–16298.

Open Access Article. Published on 26 November 2024. Downloaded on 11/27/2024 7:48:42 AM.
This article is licensed under a Creative Commons Attribution-NonCommercial 3.0 Unported Licence.



Data availability statement:

View Article Online
DOI: 10.1039/D4TA02807D

The data supporting this article have been included as part of the Supplementary Information

